

## Article

# Radio and X-ray Observations of the Restarted Radio Galaxy in the Galaxy Cluster CL 0838+1948

Simona Giacintucci , Tracy Clarke , Namir E. Kassim , Wendy Peters  and Emil Polisensky 

Naval Research Laboratory, 4555 Overlook Avenue SW, Code 7213, Washington, DC 20375, USA; tracy.clarke@nrl.navy.mil (T.C.); namir.kassim@nrl.navy.mil (N.E.K.); wendy.peters@nrl.navy.mil (W.P.); emil.polisensky@nrl.navy.mil (E.P.)

\* Correspondence: simona.giacintucci@nrl.navy.mil

**Abstract:** We present VLA Low-band Ionosphere and Transient Experiment (VLITE) 338 MHz observations of the galaxy cluster CL 0838+1948. We combine the VLITE data with Giant Metrewave Radio Telescope 610 MHz observations and survey data. The central galaxy hosts a 250 kpc source whose emission is dominated by two large lobes at low frequencies. At higher frequencies, a pair of smaller lobes ( $\sim 30$  kpc) is detected within the galaxy optical envelope. The observed morphology is consistent with a restarted radio galaxy. The outer lobes have a spectral index  $\alpha_{\text{out}} = 1.6$ , indicating that they are old, whereas the inner lobes have  $\alpha_{\text{inn}} = 0.6$ , typical for an active source. Spectral modeling confirms that the outer emission is a dying source whose nuclear activity switched off not more than 110 Myr ago. Using archival *Chandra* X-ray data, we compare the radio and hot gas emission. We find that the active radio source is contained within the innermost and X-ray brightest region, possibly a galactic corona. Alternatively, it could be the remnant of a larger cool core whose outer layers have been heated by the former epoch of activity that has generated the outer lobes.

**Keywords:** radio galaxies; active galactic nuclei; galaxy clusters



**Citation:** Giacintucci, S.; Clarke, T.; Kassim, N.E.; Peters, W.; Polisensky, E. Radio and X-ray Observations of the Restarted Radio Galaxy in the Galaxy Cluster CL 0838+1948. *Galaxies* **2021**, *9*, 108. <https://doi.org/10.3390/galaxies9040108>

Academic Editors: Francesca Loi and Tiziana Venturi

Received: 29 September 2021  
Accepted: 16 November 2021  
Published: 21 November 2021

**Publisher's Note:** MDPI stays neutral with regard to jurisdictional claims in published maps and institutional affiliations.



**Copyright:** © 2021 by the authors. Licensee MDPI, Basel, Switzerland. This article is an open access article distributed under the terms and conditions of the Creative Commons Attribution (CC BY) license (<https://creativecommons.org/licenses/by/4.0/>).

## 1. Introduction

In a growing number of radio galaxies, the combination of sensitive, high-resolution images at low ( $<1$  GHz) and higher frequencies provides evidence that the central active galactic nucleus (AGN) has undergone intermittent episodes of jet activity over the source lifetime (see review by [1]). Striking examples are the so-called *double-double* radio galaxies, in which two distinct pairs of radio lobes are seen on different scales: a pair of inner lobes, that are currently sustained by the AGN jets, and a pair of outer lobes that have been inflated during a former episode of activity [2]. More generally, evidence for recurrent radio outbursts is supported by the co-existence of a small-scale radio source with a spectral index typical for an active radio galaxy ( $\alpha \sim 0.6\text{--}0.8$ <sup>1</sup>, e.g., [3]) and larger-scale, extended emission with a significantly steeper spectrum ( $\alpha \sim 1.5\text{--}2$ ), which is instead typical for dying or relic radio galaxies (e.g., [4–6]). Although the inner component is presently fed by the AGN, the outer *remnant* emission has no jets supporting the radio activity and is therefore rapidly fading, as reflected by the pronounced steepening of its radio spectrum. Eventually, radiative and adiabatic expansion losses will cause the remnant emission to fade out of the observable radio band and disappear completely. The remnant phase is expected to be relatively short (a few times  $10^7$  years), which may explain the rarity of dying and restarted radio sources among the general population of extended radio galaxies (e.g., [5,7–10]). However, our current knowledge of the properties, occurrence and environment of dying/restarted radio galaxies is mostly based on studies of individual objects or small collections (e.g., [4,11–14]), and only a few investigations have been conducted using samples selected from radio surveys (e.g., [5,8,10]) or literature [15].

An improved understanding of the statistical properties of remnant sources, and of radio galaxy evolution in general, requires larger and more representative samples of

sources. These are now becoming available (e.g., [7,9,16]) thanks to new and upcoming high-resolution surveys (e.g., LoTSS<sup>2</sup>, MGCLS<sup>3</sup>, ASKAP<sup>4</sup>) with the new generation of radio telescopes (e.g., LOFAR<sup>5</sup>, MWA<sup>6</sup>, uGMRT<sup>7</sup>, MeerKAT [23], ASKAP<sup>8</sup>).

In this paper, we present a study of the restarted radio galaxy in the galaxy cluster CL 0838+1948 (hereafter CL 0838, also known as MCXC J0838.5+1948), a relaxed cool-core cluster at  $z = 0.123$  with a bolometric X-ray luminosity of  $5.7 \times 10^{43} \text{ erg s}^{-1}$  [25]. The interesting morphology of this radio source was noted for follow-up study during routine visual inspection of the pipeline image archive of the VLA Low-band Ionosphere and Transient Experiment (VLITE), a commensal system that operates on the Very Large Array (VLA). Here, we combine the VLITE data at 338 MHz with an archival GMRT observation at 610 MHz and images from radio surveys at multiple frequencies and angular resolutions. We analyze the morphological and spectral properties of the radio source and derive its physical parameters. We use an archival *Chandra* X-ray observation to measure global properties of the intracluster medium and compare the radio and X-ray emission. We adopt  $\Lambda$ CDM cosmology with  $H_0 = 70 \text{ km s}^{-1} \text{ Mpc}^{-1}$ ,  $\Omega_m = 0.3$  and  $\Omega_\Lambda = 0.7$ . At the redshift of CL 0838,  $1''$  corresponds to 2.2 kpc.

## 2. Observations and Data Reduction

In this section, we describe the radio and X-ray observations of CL 0838 used in this paper. In the radio band, we analyze VLITE data at 338 MHz and an archival GMRT observation at 610 MHz. We also use radio data from the Galactic and Extragalactic All-Sky MWA (GLEAM) survey [26], the Very Large Array Low-frequency Sky Survey Redux (VLSSr; [27]), the TIFR GMRT Sky Survey Alternative Data Release (TGSS-ADR; [28]), the Rapid ASKAP Continuum Survey (RACS; [19]), the NRAO VLA Sky Survey (NVSS; [29]), the Faint Images of the Radio Sky at Twenty-cm (FIRST; [30]) and the Very Large Array Sky Survey (VLASS; [31]) Epoch 1.2.

### 2.1. VLITE 338 MHz Data

VLITE is a commensal system on the VLA that operates in parallel with nearly all regular observations above 1 GHz [32]. It correlates data from a 64 MHz sub-band centered on 352 MHz for a subset of VLA antennas (up to 18) using the low-band receiver system [33] and a dedicated DiFX-based software correlator [34]. Due to strong radio frequency interference (RFI) in the upper portion of the band, the usable frequency range is limited to an RFI-free band of  $\sim 40$  MHz, centered on 338 MHz.

VLITE was operational with 16 working antennas during two VLA 1.5 GHz observations of the Praesepe open cluster on 2018 January 22 (B configuration) and 2018 January 31 (BnA configuration; VLA project 17B-370; 5.6 hours/day). The galaxy cluster CL 0838 is located at  $RA_{J2000} = 8 \text{ h } 38 \text{ m } 31.3 \text{ s}$  and  $DEC_{J2000} = 19^\circ 48' 17''$  [35], which is  $34'$  away from the phase center of the Praesepe observations, and thus well within the VLITE primary beam ( $2.5^\circ$ ).

The VLITE data are processed using a dedicated calibration and imaging pipeline, which is based on a combination of Orbit [36] and AIPS [37] software packages. The pipeline uses standard automated tasks for the removal of RFI, followed by delay, complex gain, and bandpass calibration (for details see [38]). The flux density scale is set using [39] and the primary calibrators 3C147, 3C286, 3C48 and 3C138. Residual amplitude errors are estimated to be less than 15% (Clarke et al., in preparation). The calibrated data are imaged using wide-frequency imaging algorithms in Orbit (task MFImage), by covering the full primary beam with facets and placing outlier facets on bright sources out to a radius of  $20^\circ$ . Small clean masks are placed on the sources during the imaging process to reduce the effects of CLEAN bias. The pipeline runs two imaging and phase self-calibration cycles before a final image is created.

For the Praesepe field, the pipeline produced an image with a beam of  $16'' \times 14''$  and  $0.9 \text{ mJy beam}^{-1}$  rms from the January 22 observation, and an image with a beam of  $17'' \times 16''$  and rms of  $2.7 \text{ mJy beam}^{-1}$  from the January 31 data. To improve the image

quality, the two pipeline-calibrated data sets were jointly re-imaged with *wsclean* [40] using a ROBUST Briggs parameter of  $-0.5$  [41]. The final image has a restoring beam of  $13'' \times 9''$  and a rms noise level of  $1\sigma = 0.4 \text{ mJy beam}^{-1}$ . The image was corrected for the primary beam attenuation using factors appropriate for VLITE (Polisensky et al. in preparation).

## 2.2. GMRT 610 MHz Data

We analyzed an archival GMRT observation at 610 MHz that contains CL0813 in its field of view, at  $18'$  from the phase center (project 15NGA01, observation 4117). The field was observed for about 15 minutes using the old hardware correlator and both the upper and lower side bands (USB and LSB), providing a total observing bandwidth of 32 MHz. The default spectral-line mode was used. We calibrated the USB and LSB data sets individually in AIPS. A combination of RFLAG and manual flagging was used to remove RFI and bad data. After bandpass calibration and a priori amplitude calibration using the primary calibrators 3C286, several phase-only self-calibration cycles and imaging were carried out for each data set. Widefield imaging was implemented in each step of the data reduction, with 20 facets covering the primary beam area. The calibrated USB and LSB data sets were then combined together to produce the final image that has a sensitivity of  $1\sigma = 0.25 \text{ mJy beam}^{-1}$  and resolution of  $5''$ . Flux densities are given on the Perley & Butler (2017) wide-band scale. Typical residual amplitude errors at this frequency are estimated to be less than 8% (e.g., [42]), however due to uncertainties in the primary beam model at large distances from the phase center, we assume a conservative flux uncertainty of 15%.

## 2.3. Chandra X-ray Data

CL0838 was observed by *Chandra* in 2007 (ObsID 9397) with ACIS-I for 20 ks. We reprocessed the Level-1 ACIS event file from the archive using CIAO 4.8, following the procedure described in [43] and using the *Chandra* Calibration Database (CALDB) 4.6. Following [44], we inspected the data for flares, but found no time intervals with elevated background. To model the detector and sky background, we used the blank-sky datasets from the CALDB appropriate for the date of the observation, normalized using the ratio of the observed to blank-sky count rates in the 9.5–12 keV band. We also subtracted the ACIS readout artifact [45]. We used images in the 0.5–4 keV and 2–7 keV energy bands to detect the unrelated X-ray point sources, which we masked for the spectral analysis.

We extracted a spectrum of the diffuse intracluster medium and generated the instrument responses (ARF and RMF). The background spectrum was extracted for the same region from the corresponding (normalized) blank-sky data set. The cluster X-ray emission was modeled with an absorbed, single-temperature APEC model in the 0.7–7 keV energy band, with the metal abundance fixed to 0.3 solar. The absorption column density  $N_H$  was initially left free to vary. Since the best-fit  $N_H$  value was found to be consistent with that from the Leiden/Argentine/Bonn (LAB) radio survey of Galactic HI [46], we fixed it at the database value for subsequent analysis ( $N_H = 2.57 \times 10^{20} \text{ cm}^{-2}$ ).

## 3. Results

In this Section we present the radio and X-ray images of CL0838. We measure the flux density of the total emission and its components, derive their spectral index and model the integrated radio spectrum to infer the age of the radio-emitting electrons.

### 3.1. Radio Images

The VLITE 338 MHz image of CL0838 is presented in Figure 1a. The image shows an extended radio source with the largest size of  $\sim 250$  kpc. The extended emission is dominated by a pair of large radio lobes, labeled NW and SE outer lobes. These lobes are also visible in the 888 MHz image from RACS (panel b) and GMRT images at 150 MHz (TGSS-ADR) and 610 MHz (panel c). The FIRST image at 1.4 GHz and VLASS 1.2 image at 3 GHz (c,d) reveal a pair of smaller-scale ( $\sim 30$  kpc) inner lobes that are roughly co-linear with the outer lobes and embedded (at least in projection) within the galaxy's optical

envelope. The SDSS<sup>9</sup> image in (d) suggests the presence of two nuclei at the galaxy center, which are also seen in infrared images from the UKIDSS<sup>10</sup> Galactic Center Survey (GCS; a J-band image is shown in Figure 2 with VLASS contours overlaid). Their approximate location is marked by blue crosses in Figure 1d and their projected separation is  $\sim 2''$  ( $\sim 4.4$  kpc). The resolution of the available radio images is not sufficiently high to identify the radio source core and resolve the inner jets. Higher-resolution observations, coupled with an optical/infrared analysis of the galaxy, are thus necessary to investigate the link between core/jet activity and the possible dual-nuclei system in this source.

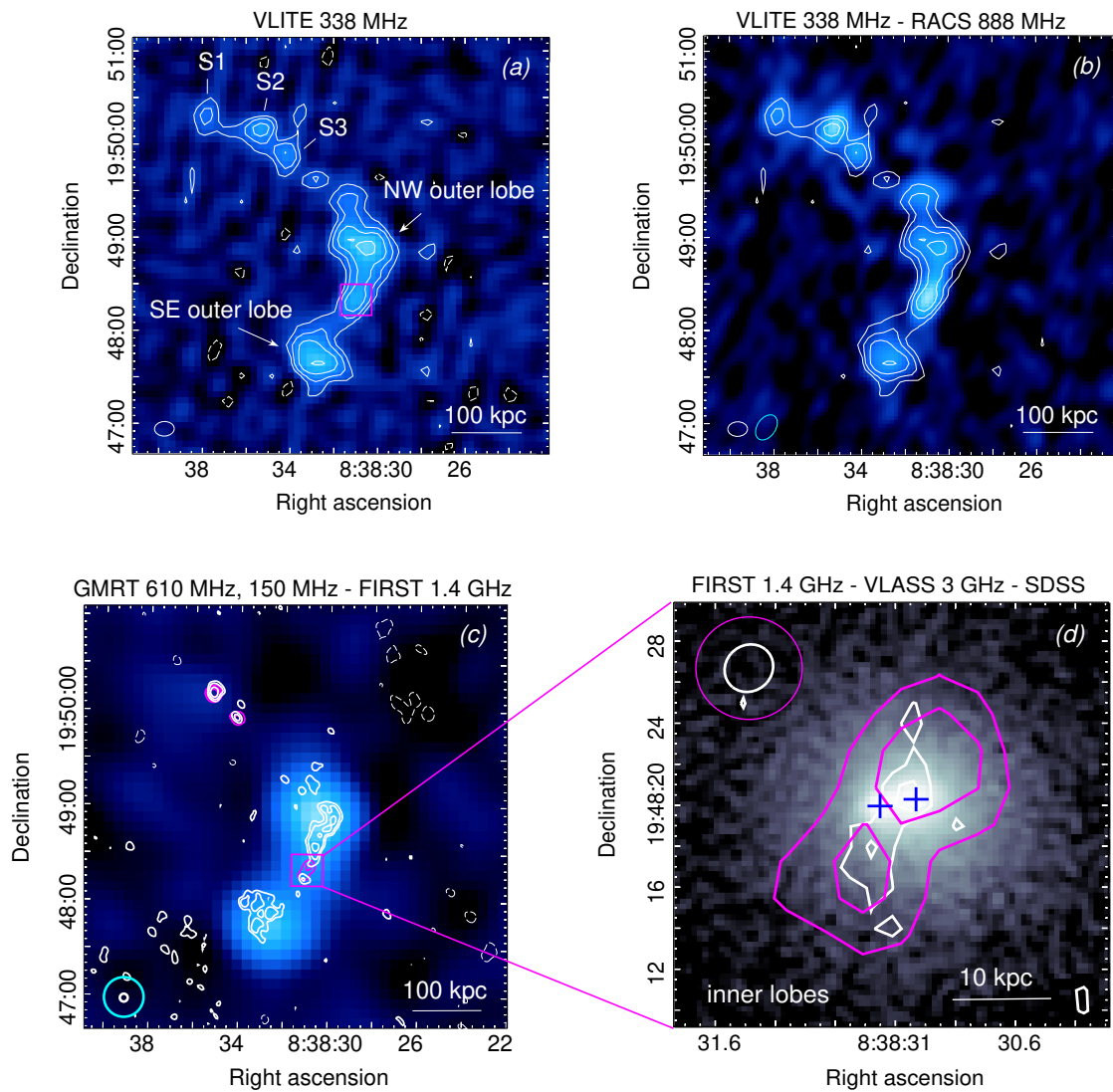


**Figure 1.** (a) VLITE 338 MHz image of CL0838 at a resolution of  $12''.7 \times 9''.4$ ,  $-88^\circ$ . Contours are spaced by a factor of 2 starting from  $+3\sigma = 1.2$  mJy beam $^{-1}$ . Contours at  $-3\sigma$  are shown as dashed. The magenta box marks the area covered by panel (d). (b) VLITE contours on the 888 MHz RACS image with a resolution of  $17''.9 \times 11''.8$ ,  $-26^\circ$  and sensitivity of  $0.25$  mJy beam $^{-1}$ . (c) GMRT 610 MHz (white) and FIRST 1.4 GHz (magenta) contours on the  $25''$ -resolution TGSS-ADR image at 150 MHz. The beam size is  $5''$  at 610 MHz and 1.4 GHz, and contours start at  $+3\sigma = 0.75$  mJy beam $^{-1}$  and  $0.45$  mJy beam $^{-1}$  respectively, and scale by a factor of 2. Negative contours are shown as dashed. (d) 1.4 GHz FIRST (magenta) and 3 GHz VLASS (white) contours on the optical SDSS-*r* image of the central galaxy. VLASS contours are  $0.33$  and  $0.46$  mJy beam $^{-1}$  (the local rms is  $1\sigma = 0.12$  mJy beam $^{-1}$ ) and the beam size is  $2''.4 \times 2''.2$ ,  $-40^\circ$ . Blue crosses mark the position of two possible optical nuclei (see also Figure 2). The radio beams are shown as ellipses/circles in each panel.

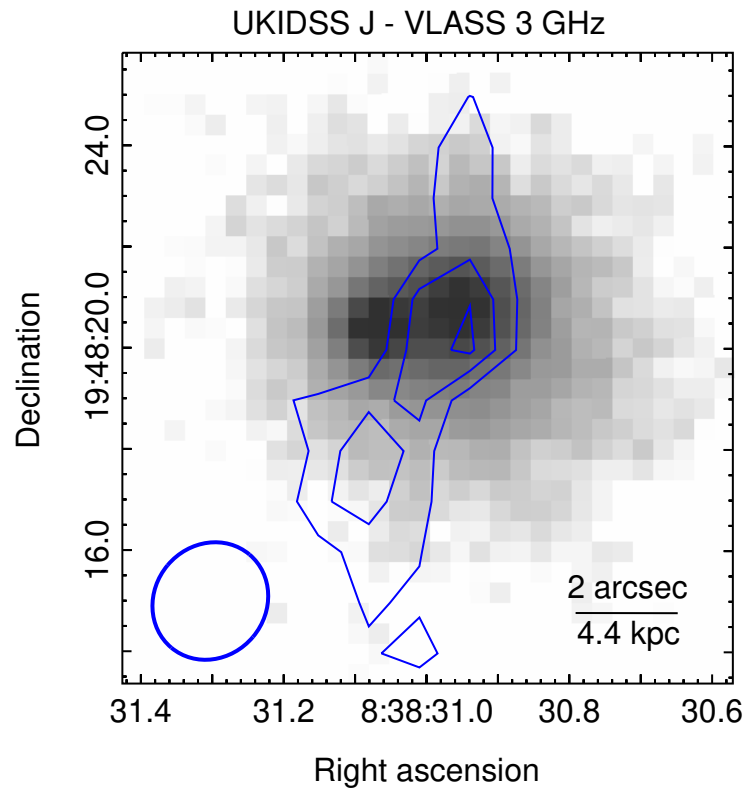


**Figure 2.** UKIDSS J-band image of the central galaxy in CL0838 showing a possible dual-nuclei system at its center (see also Figure 1d). VLASS 3 GHz contours are overlaid at 0.3, 0.4 and 0.5 mJy beam<sup>-1</sup>. The local rms in the VLASS image is  $1\sigma = 0.12$  mJy beam<sup>-1</sup>. The ellipse shows the size of the radio beam ( $2''.4 \times 2''.2, -40^\circ$ ).

A chain of three compact sources is detected North-East of the cluster center in the VLITE image. They are labeled S1, S2 and S3 in Figure 1a. S2 (RA<sub>J2000</sub> = 8 h 38 m 35.2 s, DEC<sub>J2000</sub> = 19°50'11'') and S3 (8 h 38 m 34.2 s, 19°49'55'') are both detected at 610 MHz, 888 MHz and 1.4 GHz, and are identified with two SDSS galaxies with a spectroscopic redshift of  $z_{\text{sp}} = 0.125$ , so likely cluster member galaxies. S1 has peak coordinates of 8 h 38 m 37.9 s and 19°50'18'' and has no clear optical identification (the closest galaxy is SDSS J083838.43+195014.5, which is 8''.5 away from the radio peak and has no available redshift information). This radio source is also detected by RACS and is undetected in the other radio images in Figure 1. On the left of Figure 3, we compare lower-resolution images from NVSS (45'') and RACS (25'') to the VLITE contours and optical *r*-band image from Pan-STARRS1<sup>11</sup>. On the right, we show a VLITE image at 25'' resolution. The figure suggests that S1 may be a bright peak in a larger-scale diffuse structure that extends approximately 300 kpc North-East of NW outer lobe. Hereafter, we refer to this possible further component of emission as diffuse tail.

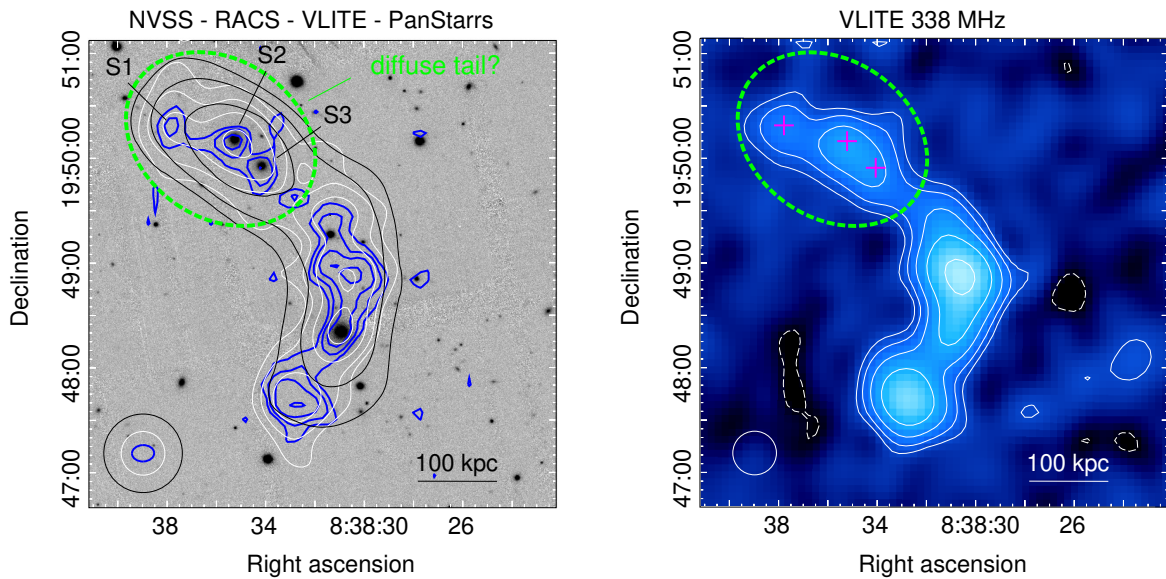


**Figure 3.** **Left:** NVSS 1.4 GHz contours (black,  $45''$  beam), RACS 888 MHz contours (white,  $25''$  beam), and VLITE 338 MHz contours (blue, from Figure 1a) overlaid on the optical  $r$ -band image from Pan-STARRS1. Contours are spaced by a factor of 2 starting from  $+3\sigma = 1.4 \text{ mJy beam}^{-1}$  (NVSS),  $0.9 \text{ mJy beam}^{-1}$  (RACS) and  $1.2 \text{ mJy beam}^{-1}$  (VLITE). **Right:** VLITE 338 MHz image at  $25''$  resolution. Contours are spaced by a factor of 2 starting from  $+3\sigma = 2 \text{ mJy beam}^{-1}$ . Negative contours ( $-3\sigma$ ) are shown as dashed. In both panels, the beam sizes are shown in the bottom-left corner. The green dashed ellipse marks the region used to measure the flux density of a possible large-scale structure (diffuse tail) extending North-East of the NW outer lobe (see Section 3.2).

### 3.2. Radio Flux Densities

We used the radio images in Figure 1 in combination with data from the VLSSr, GLEAM, RACS, NVSS, FIRST and VLASS surveys to derive the spectral index of the radio emission in CL 0838. We measured the flux density of compact sources by fitting the sources with a Gaussian model. For the extended components, we integrated the flux density over the same regions at all frequencies. Errors were computed including image rms and flux calibration uncertainty. We note that the GLEAM, VLSSr, TGSS-ADR, RACS, NVSS and FIRST surveys use a different absolute flux density scale than the [39] scale used for the VLITE, GMRT and VLASS images. We thus rescaled all flux densities to the [39] scale using the appropriate factors listed in [39]. Differences between these scales are estimated to be less than a few % [39].

Our measurements are summarized in Table 1 along with the observed spectral indices, measured between the lowest and highest frequencies available. The table also reports catalog fluxes from RACS and FIRST for S1–S3 and flux densities for the extended emission derived from the GLEAM catalog and corrected for source contamination. In fact, because of the large radio beam of the MWA, the GLEAM catalog fluxes include the contribution from S1–S3. This latter was estimated from their 338–1400 MHz spectral index (Table 1) and then subtracted from the catalog values.

Finally, we obtained an estimate of the flux density of the possible diffuse tail in Figure 3 by comparing the fluxes measured on the low- and high-resolution images at 1.4 GHz (NVSS/FIRST), 888 MHz (RACS  $25''$ /RACS  $15''$ ) and 338 MHz (VLITE  $25''$ /VLITE  $13''$ ). We measured a total flux density of  $\sim 15 \text{ mJy}$  at 1.4 GHz (NVSS) and  $\sim 23 \text{ mJy}$  at 888 MHz (RACS  $25''$ ) in the region marked by the green dashed ellipse in Figure 3. On the VLITE low-resolution image, we measured  $\sim 43 \text{ mJy}$  in the same area. We then subtracted the flux density of S1, S2 and S3 at these frequencies (Table 1) and found an excess of  $\sim 6 \text{ mJy}$  at 1.4 GHz,  $\sim 10 \text{ mJy}$  at 888 MHz, and  $\sim 20 \text{ mJy}$  at 338 MHz. The corresponding spectral index is  $\sim 0.7$  between 338 MHz and 888 MHz and  $\sim 1.1$  in the 888 MHz–1.4 GHz interval. These

estimates are very uncertain and deeper, higher-resolution observations are necessary to confirm the presence of a diffuse tail and constrain its morphology and spectral properties.

**Table 1.** Radio flux densities.

	Frequency (MHz)	Flux Density <sup>a</sup> (mJy)	Reference	Spectral <sup>b</sup> Index		
Total	74	$876 \pm 118^c$	VLSSr, this work	$1.4 \pm 0.1$		
	76	$1095 \pm 116^d$	GLEAM			
	107	$612 \pm 82^d$	GLEAM			
	143	$376 \pm 36^d$	GLEAM			
	150	$415 \pm 62$	TGSS, this work			
	174	$334 \pm 29^d$	GLEAM			
	212	$279 \pm 36^d$	GLEAM			
	338	$144 \pm 22$	VLITE, this work			
	610	$72 \pm 11$	GMRT, this work			
	888	$38 \pm 2$	RACS, this work			
	1400	$13.8 \pm 0.6$	NVSS, this work			
	Inner lobes	338	$6.7 \pm 1.1$		VLITE, this work	$0.6 \pm 0.1$
		610	$4.2 \pm 0.4$		GMRT, this work	
888		$4.0 \pm 0.3$	RACS, this work			
1400		$2.8 \pm 0.2$	FIRST, this work			
3000		$1.8 \pm 0.2$	VLASS 1.2, this work			
Outer lobes	150	$404 \pm 61^e$	TGSS-ADR, this work	$1.6 \pm 0.1$		
	338	$137 \pm 21$	VLITE, this work			
	610	$68 \pm 10$	GMRT, this work			
	888	$34 \pm 2$	RACS, this work			
	1400	$11 \pm 1$	NVSS, this work			
S1	338	$4.9 \pm 0.9$	VLITE, this work	$0.7 \pm 0.2$		
	888	$2.6 \pm 0.1$	RACS			
	1400	$1.9 \pm 0.2^f$	this work			
S2	338	$10.3 \pm 1.6$	VLITE, this work	$0.6 \pm 0.1$		
	888	$6.4 \pm 0.1$	RACS			
	1400	$4.4 \pm 0.1$	FIRST			
S3	338	$7.5 \pm 1.2$	VLITE, this work	$0.7 \pm 0.1$		
	888	$3.7 \pm 0.1$	RACS			
	1400	$2.8 \pm 0.1$	FIRST			

<sup>a</sup> all values have been rescaled to the same flux density scale [39]. <sup>b</sup> observed spectral index, measured between the lowest and highest frequency available. <sup>c</sup> measured on the VLSSr image and corrected for the clean bias ([27]). <sup>d</sup> the expected contribution of S1–S3 (based on their spectral indices at higher frequency) has been subtracted from the catalog flux density; <sup>e</sup> the contribution of inner lobes at this frequency was extrapolated from 338 MHz using  $\alpha = 0.56$  and then subtracted from the total flux. <sup>f</sup> extrapolated from lower frequencies using the spectral index.

### 3.3. Radio Spectral Analysis and Modeling

The integrated spectrum of the total emission from the radio galaxy is shown in Figure 4 (left). The flux densities from FIRST and VLASS have not been included in the plot as neither of these surveys have sufficient  $uv$  coverage at short spacings and surface brightness sensitivity to detect the whole source. Both surveys use the VLA in its B configuration which allows reliable mapping of angular scales up to  $1'$  at 3 GHz and  $2'$  at 1.4 GHz. The source size is  $\sim 2'$  (Figure 1), thus it is considerably larger than the maximum scale than can be imaged by VLASS. The FIRST survey is potentially able to image the full source; however, its surface brightness sensitivity ( $1\sigma = 150 \mu\text{Jy beam}^{-1}$ , corresponding to  $\sim 4 \mu\text{Jy arcsec}^{-2}$ ), is not high enough to detect the outer lobe emission, whose average surface brightness is  $\sim 2 \mu\text{Jy arcsec}^{-2}$  at 1.4 GHz (based on the NVSS flux density, Table 1).

The total spectrum in Figure 4 is steep, with a measured spectral index  $\alpha_{\text{tot,obs}} = 1.4 \pm 0.1$  between 76 MHz and 1400 MHz. A fit with a simple power-law model (dashed line) gives a slope of  $1.4 \pm 0.1$ , but it does not describe well the highest-frequency data

in the spectrum. A power-law model including a high-frequency exponential cutoff ( $S_\nu \propto \nu^{-\alpha} e^{-\nu/\nu_{br}}$ , black solid line) provides a better fit, with  $\alpha_{tot,fit} = 1.1 \pm 0.1$  and a break frequency  $\nu_{tot,br} = 1.3 \pm 0.4$  GHz. The spectrum of the inner lobes is shown in magenta in Figure 4. The shape is consistent with a single power law, at least over the observed 338–3000 MHz interval, with a slope  $\alpha_{inn,fit} = 0.57 \pm 0.11$ .

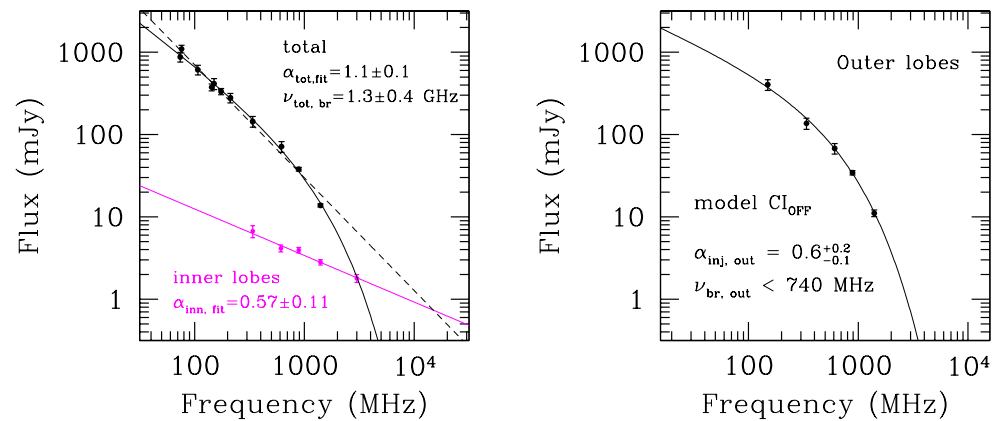


**Figure 4.** **Left:** Total radio spectrum of CL0838 between 74 MHz and 1400 MHz (black) and spectrum of the inner lobes between 338 MHz and 3000 MHz (magenta). Black lines are fits to the total spectrum data: a simple power law (black, dashed) and a power law with an exponential cutoff (black, solid). For this latter, which provides a better fit to the data, spectral index ( $\alpha_{tot,fit}$ ) and cutoff frequency ( $\nu_{tot,br}$ ) are reported. The magenta solid line is a power-law fit to the inner lobe measurements. **Right:** Radio spectrum of the outer lobes after subtraction of the inner lobes. The solid line is a  $CI_{OFF}$  fit to the fluxes (see text and Table 2).

The morphology and very steep spectral index of the source suggest that we are observing two emission components associated with two distinct phases of activity of the galaxy, i.e., fossil emission on the large scale remaining from a past outburst of the central nuclear source, and restarted activity in the flatter-spectrum inner lobes. To model the outer (fossil) component, we subtracted the flux of the inner lobes from the total emission at 338, 610, 888 and 1400 MHz (Table 1). We also estimated the inner lobe flux density at 150 MHz using their spectral index and subtracted it from the total emission measured from the TGSS-ADR. Due to the much coarser angular resolution and uncertainties on source contamination, we did not attempt a similar subtraction at the GLEAM and VLSSr frequencies.

The measured 74–1400 MHz total spectral index of the outer lobes is very steep,  $\alpha_{out,obs} = 1.6 \pm 0.8$ . Their integrated spectrum is shown in Figure 4 (right), where a steepening at high frequencies is clearly visible. We modeled the spectrum using a  $CI_{OFF}$  model that assumes (1) an initial phase of electron injection at a constant rate by the nuclear source (i.e., the continuous injection or CI phase), (2) a switch-off phase of the nuclear activity, and (3) a *dying* phase, during which the radio emission rapidly fades (for details see [5,8]). In this model, the radiative energy losses are assumed to be dominant with respect to other processes (e.g., adiabatic losses). It is also assumed that the magnetic field strength is uniform within the whole source volume and the electron pitch angles are continually isotropized with respect to the local direction of the magnetic field in a time that is shorter than the radiative timescale. For CL 0838, we found that the spectrum can be modeled with an injection spectral index of  $\alpha_{inj,out} = 0.6$  and a break frequency  $\nu_{br,out} \lesssim 740$  MHz. Our results are summarized in Table 2.

**Table 2.** Radio spectral modeling results and radiative ages.

Component	$\alpha_{\text{inj}}$	$\nu_{\text{br}}$ (MHz)	$t_{\text{rad}}$ (Myr)	$t_{\text{OFF}}/t_{\text{rad}}$	$t_{\text{CI}}$ (Myr)	$t_{\text{OFF}}$ (Myr)
inner lobes	...	$\gtrsim 3000$	$\lesssim 52$	...		
outer lobes	$0.6^{+0.2}_{-0.1}$	$\lesssim 740$	$\gtrsim 122$	$\lesssim 0.9$	$\gtrsim 12$	$\lesssim 110$

### 3.4. Equipartition Parameters and Radiative Ages

We calculated the physical parameters of the inner and outer lobes under the assumption that the relativistic particle and magnetic field energy densities are uniformly distributed over the source volume and are in energy equipartition. We assumed cylindrical geometry, a filling factor of 1, and  $k = 1$  (i.e., that there is equal energy in relativistic ions and electrons), and imposed a low-energy cutoff of  $\gamma_{\text{min}} = 100$  in the energy distribution of the radio-emitting electrons to take into account the contribution from relativistic electrons with an energy as low as 50 MeV (e.g., [50,51]). We used the measured radio luminosity at 338 MHz, the injection spectral index  $\alpha_{\text{inj, out}} = 0.6$  for the outer lobes and  $\alpha_{\text{inj, fit}} = 0.6 \pm 0.1$  for the inner lobes. We obtained  $B_{\text{eq, out}} = 2.1 \mu\text{G}$  (outer lobes) and  $B_{\text{eq, inn}} = 4.3 \mu\text{G}$  (inner lobes). We also derived the total energy density and minimum pressure of both components. Results are summarized in Table 3.

Finally, we used the equipartition magnetic field in combination with the break frequency limits from the spectral modeling to estimate the synchrotron age of the outer lobes (e.g., from Equation 8 in [5]). We obtained  $t_{\text{rad, out}} \gtrsim 122$  Myr, confirming that the outer lobe emission is very old. The  $CI_{\text{OFF}}$  model also allows us to estimate the dying-to-total source age ratio,  $t_{\text{OFF}}/t_{\text{rad}}$  [8]. In the case of CL0838, we find that the duration of the dying phase is no more than 110 Myr old and that the prior phase of activity had lasted at least 12 Myr. For the inner lobes, whose spectrum does not show a break at the observed frequencies, we can derive an upper limit to their radiative lifetime by assuming that the spectral break is  $\gtrsim 3$  GHz. We find  $t_{\text{rad, inn}} \lesssim 52$  Myr. Our results are summarized in Table 2.

**Table 3.** Physical parameters

Component	$L_{338 \text{ MHz}}$ (W Hz <sup>-1</sup> )	$B_{\text{eq}}$ ( $\mu\text{G}$ )	$u_{\text{min}}$ (erg cm <sup>-3</sup> )	$P_{\text{min}}$ (erg cm <sup>-3</sup> )	$P_{\text{gas}}$ (erg cm <sup>-3</sup> )
inner lobes	$2.6 \times 10^{23}$	4.3	$1.7 \times 10^{-12}$	$5.7 \times 10^{-13}$	$\sim 2 \times 10^{-11}$
outer lobes	$5.4 \times 10^{24}$	2.1	$4.1 \times 10^{-13}$	$1.4 \times 10^{-13}$	$\sim 1 \times 10^{-10}$

### 3.5. Chandra X-ray Analysis

Ref. [25] used *Chandra* X-ray data to investigate scaling relations between X-ray luminosity and temperature in a statistically complete subset of the 400 deg<sup>2</sup> survey [35] that includes CL0838. Using dynamical properties estimators (e.g., cuspleness of the gas density profile, core flux ratio, and a visual classification of the X-ray morphology) they characterized CL0838 as a relaxed, cool-core cluster. Here, we use the same *Chandra* data to obtain images of the thermal gas distribution and compare them to the radio emission. We also derive the average intracluster medium temperature and gas density profile.

#### 3.5.1. X-ray Images

Figure 5a shows the *Chandra* X-ray image of CL0838 in the 0.5–4.0 keV band, smoothed with a 5'' Gaussian. The X-ray emission appears regular and symmetrical on the large scale, with a bright and peaked central core, consistent with the classification of CL0838 as a relaxed cluster [25]. The 338 MHz extended emission, shown in contours in Figure 5a, is centrally located with the outer lobes extending well beyond the central, brightest X-ray region. In the center (Figure 5b), the inner lobes are contained within a very bright and compact region with a radius of  $r \sim 15$  kpc, which is co-spatial with the galaxy stellar

envelope (cyan contours). Two X-ray point sources are associated with the compact radio galaxies S2 and S3. A third bright point source is detected west of S3 and is associated with an optical SDSS object classified as a star (SDSS J083831.34+194957.9).

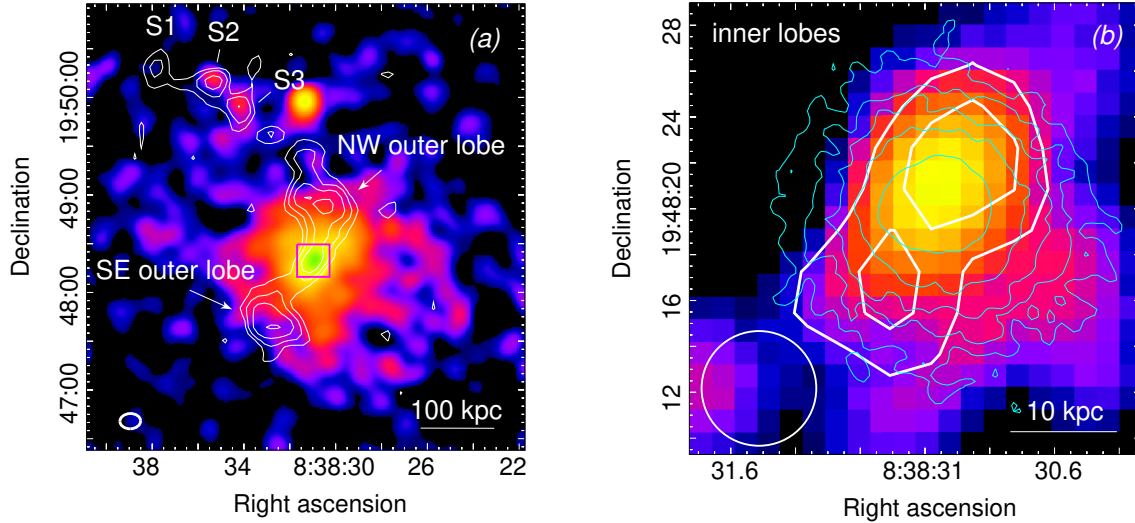


**Figure 5.** (a) VLITE 338 MHz contours overlaid on the *Chandra* X-ray image of CL0838 in the 0.5–4.0 keV band. The *Chandra* image is binned by 2 pixels (1''), background-subtracted, divided by the exposure map, and smoothed by a 5'' Gaussian. The radio beam is shown in the bottom-left corner. The magenta box marks the area covered by the inner radio lobes (panel b). (b) *Chandra* image of the central cluster region smoothed by a 2'' Gaussian. White contours are the 1.4 GHz emission from FIRST and in cyan are optical contours from the SDSS-*r* image in Figure 1d. The white circle shows the size of the radio beam.

### 3.5.2. Global Cluster Temperature and Mass

We measured the average cluster temperature as described in Section 2.3. We used a region with a radius of  $r = 340'' = 750$  kpc, which corresponds approximately to  $R_{500}^{12}$ . We found  $kT_{\text{tot}} = 3.43_{-0.54}^{+0.75}$  keV. We also measured the *core-excised* global temperature using a spectrum extracted from an annulus with  $0.15R_{500} < r < R_{500}$ . We obtained  $kT_{\text{tot,ce}} = 3.28_{-0.34}^{+0.45}$  keV, consistent with the temperature measured by [25]. Using  $kT_{\text{tot,ce}}$  and the  $M_{500} - T$  relation in [52], we estimate a total cluster mass of  $M_{500} = 2.1 \times 10^{14} M_{\odot}$ .

### 3.5.3. Gas Density Profile

We used a background-subtracted, exposure-corrected image in the 0.7–2 keV band to extract a radial surface brightness profile within  $R_{500}$ , centered on the cluster X-ray centroid. Because of the presence of a bright central core, we fit the brightness profiles by projecting a spherically symmetric double  $\beta$ -model (that better describes the gas density profile of clusters with a central cool core, e.g., [53])

$$n_e(r) = \frac{n_0}{1+f} \left[ \left( 1 + \frac{r^2}{r_{c1}^2} \right)^{-\frac{3}{2}\beta_1} + f \left( 1 + \frac{r^2}{r_{c2}^2} \right)^{-\frac{3}{2}\beta_2} \right], \quad (1)$$

where  $n_0$  (central density for the sum of the two components),  $r_{c1}$ ,  $r_{c2}$  (core radius of first and second component),  $\beta_1$ ,  $\beta_2$  (index of first and second component), and  $f$  (normalization) were free parameters. The resulting gas density profile and best-fit model are shown in Figure 6. The best-fit values are  $n_0 = 0.03 \text{ cm}^{-3}$ ,  $r_{c1} = 20.3$  kpc,  $r_{c2} = 38.9$  kpc,  $\beta_1 = 3.0$ ,  $\beta_2 = 0.5$ , and  $f = 0.03$ . A single  $\beta$ -model (not shown here) provides a good description of the profile at  $r > 15$  kpc, but fails to fit the profile at smaller radii, where a central compact region encloses the brightest extended X-ray emission seen in the *Chandra* image

(Figure 5b). This component appears to be contained within the optical extended envelope of the central galaxy, shown as cyan contours.

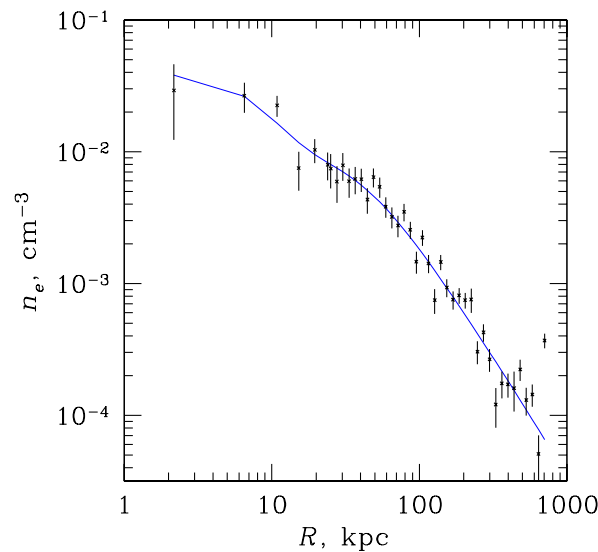


**Figure 6.** *Chandra* X-ray density profile of CL 0838. Blue solid line shows the best-fit double  $\beta$ -model.

#### 4. Discussion

Our morphological and spectral study of the extended radio emission in CL 0838 indicates that its central galaxy hosts a young radio source, but it has undergone a former episode of activity in the past. The young source consists of a pair of small lobes ( $\sim 30$  kpc) contained within the optical envelope of the galaxy. Their spectral index ( $\alpha_{\text{inn,fit}} = 0.6$ ) is typical for an active radio source, suggesting that the emission is presently sustained by the nuclear activity. However, neither the radio core nor the jets are resolved in the available radio images and higher-resolution observations are necessary to confirm that the source is currently active. Steep-spectrum ( $\alpha_{\text{out,obs}} = 1.6$ ) fossil plasma, left by the former radio outburst, is seen on the larger scale ( $\sim 250$  kpc), where a pair of unfed radio lobes dominates the emission at low frequencies. This configuration makes CL 0838 another example of a *restarted* radio galaxy. Its size is within the range typically observed for other known restarted radio galaxies, which can span from a total of  $\sim 100$  kpc to Mpc scale, with the inner doubles ranging from tens of pc to several hundred kpc (e.g., [1,54]). The total radio power ( $P_{\text{tot},150\text{MHz}} = 1.6 \times 10^{25}$  W Hz $^{-1}$ ) and spectral indices of the inner and outer lobes are also within the observed distributions (e.g., [7,54]).

Modeling of the integrated spectra of the outer lobes indicates that the remnant radio plasma is no more than  $t_{\text{off}} \sim 110$  Myr old and that the prior active phase had lasted at least 12 Myr. For the inner lobes, we derived an upper limit of 52 Myr to their radiative lifetime. We caution that these estimates are upper limits to the real ages, as we assumed that radiative losses dominate over expansion losses, and that the magnetic field intensity remains constant over the source lifetime.

##### 4.1. A Diffuse Radio Tail Hinting at Jet Precession?

In addition to the lobe emission, low-resolution images of CL 0838 suggest the presence of a further component of extended emission in the form of a  $\sim 300$  kpc diffuse tail North-East of the cluster center. This emission might be associated with one of the two (or both) optically identified cluster radio sources located in this region (S2 and S3). Alternatively, it may be connected to the restarted radio galaxy itself (i.e., it could be part of a large-scale S-shaped structure beyond the 250 kpc scale of the outer lobes). Deeper, higher-resolution radio data are needed to confirm this diffuse tail and to elucidate its possible relation to the restarted radio galaxy.

If the tail is part of the restarted radio galaxy, the total source size would almost double ( $\sim 550$  kpc). Furthermore, the lobe axis would be largely misaligned (by  $\sim 90^\circ$ ) with respect to the tail. Such misalignment could hint at precession of the jet axis (e.g., [55]). Among the mechanisms that may lead to a reorientation of the radio jets, the presence of a binary supermassive black hole has been proposed as a possible driver of jet misalignment in some double-double radio galaxies (e.g., [56]) and of jet reorientation in X-shaped radio sources ([57]). More generally, the presence of a black-hole binary may be responsible for the recurrent activity itself in double-double sources (e.g., [58]). In this regard, it is noteworthy that the optical and infrared images of the central galaxy in CL 0838 suggest the presence of a kpc-scale binary nuclei system at its center. However, the current radio images do not allow us to identify the position of the radio core and resolve the inner jets, and higher-resolution observations, coupled with an optical/infrared analysis, are needed to investigate in detail the link between the radio activity and the two possible nuclei.

#### 4.2. Radio/X-ray Interaction

The effects of the propagation of radio jets and lobes through the surrounding thermal medium can often be seen directly in the X-ray images in the form of surface brightness depressions (cavities), rims and shocks created by the radio plasma as it displaces and pushes away the X-ray emitting gas (e.g., [59,60]). X-ray cavities are commonly detected in the densest, innermost regions of cool-core clusters and groups (e.g., [61–63]), where the X-ray surface brightness contrast is high. Outside the cores, the brightness contrast is much lower and for this reason large-scale cavities have been detected only in a few systems with sufficiently deep X-ray exposures (e.g., [64–66]). There is general consensus that the energy released by the AGN jets as they evacuate cavities can suppress catastrophic cooling of thermal gas in the cores of clusters and groups as well as in isolated giant elliptical galaxies (e.g., reviews by [67,68]).

To search for X-ray cavities and other features associated with the inner and outer lobes of CL 0838, we inspected the *Chandra* images in Figure 5 as well as X-ray residual maps obtained after subtraction of a best-fit surface brightness model to the cluster emission (images not shown here). We found no evidence for cavities at the inner and outer lobes (Figure 5); however, the current *Chandra* image is too shallow to reliably identify any potential cavities. Even if we assume the presence of cavities entirely void of thermal gas at the lobe locations, the expected surface brightness decrement would be undetectable given the statistical errors on the flux in the presumed cavity regions ( $1\sigma = 20\%$  in the inner lobe region and  $1\sigma = 13\%$  in the region occupied by the outer lobes). Deeper X-ray observations (of the order of about 10 times deeper) are needed to shed light on the presence or absence of X-ray cavities in this cluster. A non-detection of clear cavities (if not explained by projection effects, e.g., [69]) may have important implications for the content of the radio lobes. In particular, it could suggest that the lobes are only partially filled by relativistic plasma and contain significant amount of hot thermal material, for instance entrained by the radio jets and transported into the lobes (e.g., [70]).

#### 4.3. Outburst Energy

The total energy output of a radio source is known to be dominated by the mechanical work done by the AGN jets on the surrounding thermal gas. In systems with X-ray cavities, it is possible to directly infer the mechanical power of the radio jets that have evacuated the X-ray cavities (e.g., [67]). If the system has multiple pairs of cavities, generated during different outbursts of the central galaxy, then it is possible to compare the energy output associated with the different cycles of activity. In some clusters, it is found that the new activity is more energetic than the past one, implying that the mean jet power must have increased significantly with time (e.g., [12]). In other systems, on the contrary, the past activity is found to be the most energetic (e.g., [66,71]), although the current epoch of activity is still ongoing, and the jet power may increase.

Due to the lack of X-ray cavities associated with the lobes in CL0838, we cannot compare the jet mechanical energy during the two phases of activities. Even though it accounts for only a small part of the radio source total energy, we can compare the energy released via synchrotron radiation during the two epochs of activity. Based on the radiative age limits (Section 3.3) and bolometric (10 MHz–100 GHz) luminosities of  $\sim 2 \times 10^{41} \text{ erg s}^{-1}$  and  $\sim 2 \times 10^{40} \text{ erg s}^{-1}$  for the outer and inner lobes respectively (calculated as in [72]), we find that the past outburst has radiated  $\gtrsim 7.7 \times 10^{56} \text{ erg}$  over its lifetime of at least 122 Myr (i.e.,  $\gtrsim 6.3 \times 10^{54} \text{ erg Myr}^{-1}$  on average), of which  $\gtrsim 7.6 \times 10^{55}$  during its active phase ( $\gtrsim 12 \text{ Myr}$ ); the younger source has instead released no more than  $\sim 3.3 \times 10^{55} \text{ erg}$  in  $\lesssim 52 \text{ Myr}$  (i.e.,  $\lesssim 6.3 \times 10^{53} \text{ erg Myr}^{-1}$ ). This may indicate that the AGN total energy output has decreased with time, if the mean jet mechanical power has not changed significantly over the source history. However, if the AGN is currently active, its mechanical power may increase with time.

#### 4.4. Cluster Environment

Dying (including restarted) radio galaxies are found to account for only a small fraction of the radio galaxy population (<10–15%, e.g., [7,9,16]). This is believed to be a consequence of the short fading timescales (a few  $10^7$  years) of the remnant phase caused by radiative and adiabatic expansion losses. However, there is indication that the fraction of dying radio sources may increase when considering only sources in galaxy clusters [8], with a probability for a dying source to be found in a cluster as high as  $\sim 86\%$  [5]. However, these studies were based on a small number of objects and other recent investigations (e.g., [7]) found that most of the remnant and restarted radio sources do not seem to reside in rich clusters. A larger and more systematic study of dying/restarted radio sources is needed to draw firm conclusions on the effect of the environment on their evolution. If a preference for denser environment is confirmed, this would suggest that the lifetime of a radio source may be affected by the medium in which the galaxy resides, especially after the cessation of the nuclear activity. One possibility is that the high pressure exerted by the dense intracluster medium on the radio lobes may reduce the expansion losses and thus extend their lifetime (and, consequently, their detectability at low radio frequencies). In this regard, the restarted radio source studied here may fit this scenario, as it is embedded in a very dense thermal environment such as the center of a cool-core cluster.

#### 4.5. Thermal/Non-Thermal Pressure Comparison

Using our best-fit double  $\beta$ -model to the density gas profile and cluster core-excised temperature, we obtained an order-of-magnitude estimate of the thermal gas pressure at the average radius of the outer lobes ( $r \sim 100 \text{ kpc}$ ) as  $P_{\text{gas}} \simeq 2.25 n_{\text{H}} k T$ , where the proton density  $n_{\text{H}}$  is related to the electron density as  $n_{\text{e}} = 1.17 n_{\text{H}}$ . We obtained  $P_{\text{gas}} \sim 2 \times 10^{-11} \text{ erg cm}^{-3}$ , which is two orders of magnitude larger than the radio plasma pressure estimated under the minimum energy condition hypothesis (Section 3.4, Table 2). Similarly, we found a large pressure unbalance for the inner lobes ( $r \sim 15 \text{ kpc}$ ), where  $P_{\text{gas}} \sim 1 \times 10^{-10} \text{ erg cm}^{-3}$ , while the non-thermal pressure is only  $P_{\text{min,inn}} = 5.7 \times 10^{-13} \text{ erg cm}^{-3}$  (Table 2).

A similar lack of pressure balance has been reported for other cluster and group central radio galaxies (e.g., [73]), including dying/restarted radio galaxies (e.g., [4,74,75]). It suggests a departure from the minimum energy condition within the radio-emitting plasma, i.e., a higher relativistic particle or magnetic field energy density within the radio lobes. Alternatively, the pressure equilibrium may be restored if the volume filling factor of the radio plasma is  $< 1$  (for instance in the presence of a highly filamentary magnetic fields within the lobes) and/or  $k \gg 1$ , i.e., the lobes may contain a population of non-radiating relativistic particles (protons) that are energetically dominant and contribute to the internal pressure. For CL0838, achieving pressure balance would require a proton-to-electron energy ratio  $k > 1000$  in the outer lobes, which is very large. We note, however, that similar values have been reported also for other cluster radio sources (e.g., [61]). Finally, entrainment of hot thermal plasma by the jets during their propagation through

the surrounding medium (e.g., [76]) might also provide additional pressure support in the lobes to counterbalance the external pressure.

#### 4.6. Galactic Corona or Cool-Core Remnant?

The *Chandra* X-ray image and density profile reveal the presence of a very compact inner region ( $r < 15$  kpc) that encloses the brightest X-ray emission and is co-spatial with the extended optical envelope of the central galaxy. This suggests that this component could be thermal emission from a galactic corona, as seen in several cluster and group elliptical galaxies (e.g., [77]). An alternative possibility is that this component is the *remnant* of a pre-existing, larger-scale cool core whose outermost layers have been heated by the central AGN activity (as it was suggested for the cluster associated with the radio source PKS 1353–341, [78]; see also [79]). In such a scenario, this AGN activity could be the same past episode that has inflated the outer radio lobes, whose location is in fact well beyond the inner compact core. Spatially resolved brightness and spectral analysis at small radii would provide details on size and thermodynamic properties of this component, and thus help to distinguish between an interstellar medium vs. intracluster medium nature. However, photon statistics from the current *Chandra* data are insufficient to reliably measure the gas temperature in this region and verify that it is a physically distinct emission component.

## 5. Conclusions

We presented VLITE observations at 338 MHz of the central radio galaxy in the cluster CL 0838. Combining the VLITE data with an archival GMRT observation at 610 MHz and survey data, we studied the morphological and spectral properties of the radio source and its components and derived their physical parameters. We used an archival *Chandra* X-ray observation to measure global properties of the intracluster medium (temperature and density profile) and compare the radio and X-ray emission. Our main results are summarized below:

- the cluster central galaxy hosts an extended radio source (250 kpc), whose radio emission is composed of a pair of large and steep-spectrum ( $\alpha_{\text{out,obs}} = 1.6$ ) outer lobes and two smaller-scale (30 kpc) inner lobes characterized by a much flatter spectral index ( $\alpha_{\text{inn,fit}} = 0.6$ ). The combination of morphology and different spectral indices suggests that the source is a restarted radio galaxy: the inner lobes are associated with a young radio source, whereas the outer lobes are fossil emission remaining from a former episode of activity;
- modeling of the integrated spectrum using a *dying* radio source ( $\text{CI}_{\text{OFF}}$ ; e.g., [8]) model supports a scenario in which the outer lobes are the remnant of a past AGN outburst. Under equipartition assumptions, we estimated that their synchrotron emission is no more than 110 Myr old and that the prior phase of activity had lasted at least 12 Myr. For the inner lobes, whose spectral shape is typical for an active radio source, we estimated that they are younger than 52 Myr;
- a possible tail of diffuse emission, misaligned with respect to the lobe axis, is detected North-East of the cluster center. If associated with the restarted radio galaxy, this misaligned tail may hint at jet precession. The optical and infrared images of the central galaxy suggests the presence of two distinct nuclei,  $\sim 4$  kpc apart. The precession of the jet axis may be linked to this candidate binary system. However, more radio data are needed to confirm the diffuse tail and resolve the core and inner jets in the center to determine their relation to the dual-nuclei system;
- the *Chandra* images show that the cluster is relaxed. The radio galaxy is centrally located, and its outer lobes extend beyond the central core, while the inner lobes are contained within the innermost and brightest X-ray region;
- we measured a cluster average temperature (core-excised) of 3.28 keV and estimated a mass of  $M_{500} = 2.1 \times 10^{14} M_{\odot}$  from the  $M_{500}-T$  relation;
- the intracluster gas density profile is well described by a double  $\beta$ -model, while a single  $\beta$ -model is not able to reproduce the observed profile at  $r < 15$  kpc. This region

is associated with a compact component in the X-ray images, which encloses the brightest X-ray emission, and is contained within the optical extended envelope of the central galaxy. It is possible that this component is thermal emission arising from a galactic corona. Alternatively, it could be a cool-core *remnant* left after the outermost regions of a pre-existing, larger-scale cool core have been heated up by the AGN activity. This activity could be the same past outburst that has generated the radio lobes outside the compact core. The current *Chandra* exposure provides insufficient photon statistics to reliably image the small-scale structure of this central compact core and measure its temperature. Deeper observations are needed to examine in detail the structure and thermodynamic properties of this component and shed light on its interstellar *vs* intracluster medium origin;

- the *Chandra* images show no X-ray cavities or other substructures associated with the radio source. The possible lack of cavities may suggest that the radio lobes contain a significant amount of hot thermal gas (for instance, entrained and transported by the radio jets). However, deeper X-ray observations are needed to confirm the lack of cavities in this system;
- due to the lack of X-ray cavities, we were not able to investigate the evolution of the mean jet mechanical energy between the two epochs of AGN activity that have created the inner and outer lobes. We were able to compare the energy radiated as synchrotron emission, which is believed to be only a small fraction of the total energy of a radio source. We found that the past outburst has radiated an energy of at least  $\sim 1.6 \times 10^{57}$  erg, whereas the younger activity has released no more than  $\sim 3.3 \times 10^{55}$  erg. If the mean jet mechanical power has not changed significantly over the source history, this may indicate that the AGN total energy output has decreased between the two epochs of activity. However, if the current epoch of activity is still ongoing, it is possible that the mechanical power may become larger.
- the restarted radio galaxy studied here resides in the center of a cool-core cluster [25], which is a very dense thermal environment. Other dying/restarted sources have been found at cluster or group centers (e.g., [75]); however, it is still unclear whether these sources preferentially reside in dense environments [7]. In the dense cores of groups and clusters, such as CL0838, the high thermal pressure of the external gas may be able to confine the lobes and reduce the energy losses caused by adiabatic expansion, thus extending the lobes lifetime compared to a dying source in a less dense environment;
- comparison of the lobe internal pressure, computed under the assumption of minimum energy conditions, to a rough order-of-magnitude estimate of thermal gas pressure indicates a pressure unbalance of two orders of magnitude for both pairs of lobes. This implies that an additional contribution to the lobe pressure, for instance from non-radiating relativistic particles or hot thermal material in the lobes, is needed to maintain pressure balance (assuming that the source is not significantly far from equipartition conditions between relativistic particle and magnetic field energy densities).

Looking forward, high-sensitivity ongoing and future radio surveys with instruments such as LOFAR, ASKAP, MeerKAT, uGMRT, VLITE, and MWA will provide new opportunities to build larger samples of restarted radio galaxies to improve our understanding of these systems and of their environment.

**Author Contributions:** Conceptualization and methodology; S.G., T.C.; software and analysis; W.P., E.P., S.G.; writing—review and editing; S.G., T.C., N.E.K., W.P., E.P. All authors have read and agreed to the published version of the manuscript.

**Funding:** Basic research in radio astronomy at the U.S. Naval Research Laboratory is supported by 6.1 Base funding.

**Institutional Review Board Statement:** Not applicable.

**Informed Consent Statement:** Not applicable.

**Data Availability Statement:** The VLITE data are available on request from the authors. Publicly available GMRT archival data and survey data from VLSSr, MWA/GLEAM, RACS, NVSS, FIRST and VLASS were analyzed in this study.

**Acknowledgments:** We thank the anonymous referees for their useful comments that have improved this work. Basic research in radio astronomy at the U.S. Naval Research Laboratory is supported by 6.1 Base Funding. Construction and installation of VLITE was supported by the NRL Sustainment Restoration and Maintenance fund. The National Radio Astronomy Observatory is a facility of the National Science Foundation operated under cooperative agreement by Associated Universities, Inc. The scientific results reported in this article are based on data obtained from the GMRT Data Archive. We thank the staff of the GMRT that made the observations possible. GMRT is run by the National Centre for Astrophysics of the Tata Institute of Fundamental Research. This scientific work makes use of the data from the Murchison Radio-astronomy Observatory and Australian SKA Pathfinder, managed by CSIRO. Support for the operation of the MWA and ASKAP is provided by the Australian Government (NCRIS). ASKAP and MWA use the resources of the Pawsey Supercomputing Centre. Establishment of ASKAP, MWA and the Pawsey Supercomputing Centre are initiatives of the Australian Government, with support from the Government of Western Australia and the Science and Industry Endowment Fund. We acknowledge the Wajarri Yamatji people as the traditional owners of the observatory sites. The scientific results reported in this article are based on data obtained from the Chandra Data Archive (ObsID 9397). This research has made use of software provided by the Chandra X-ray Center (CXC) in the application packages CIAO. This research has made use of the NASA/ IPAC Extragalactic Database (NED), which is operated by the Jet Propulsion Laboratory, California Institute of Technology. This research has made use of the CIRADA cutout service at URL [cutouts.cirada.ca](http://cutouts.cirada.ca), operated by the Canadian Initiative for Radio Astronomy Data Analysis (CIRADA). CIRADA is funded by a grant from the Canada Foundation for Innovation 2017 Innovation Fund (Project 35999), as well as by the Provinces of Ontario, British Columbia, Alberta, Manitoba and Quebec, in collaboration with the National Research Council of Canada, the US National Radio Astronomy Observatory and Australia's Commonwealth Scientific and Industrial Research Organisation.

**Conflicts of Interest:** The authors declare no conflict of interest. The funders had no role in the design of the study; in the collection, analyses, or interpretation of data; in the writing of the manuscript, or in the decision to publish the results.

## Notes

- 1 The radio spectral index  $\alpha$  is defined according to  $S_\nu \propto \nu^{-\alpha}$ , where  $S_\nu$  is the flux density at the frequency  $\nu$ .
- 2 LOFAR Two-metre Sky Survey [17].
- 3 MeerKAT Galaxy Cluster Legacy Survey [18].
- 4 Rapid ASKAP Continuum Survey [19].
- 5 LOw-Frequency ARray [20].
- 6 Murchison Widefield Array [21].
- 7 upgraded Giant Metrewave Radio Telescope [22].
- 8 Australian Square Kilometre Array Pathfinder [24]
- 9 Sloan Digital Sky Survey [47].
- 10 UKIRT Infrared Deep Sky Survey [48].
- 11 Panoramic Survey Telescope and Rapid Response System [49]
- 12  $R_{500}$  is the radius that encloses a mean overdensity of 500 with respect to the critical density at the cluster redshift.

## References

1. Saikia, D.J.; Jamrozy, M. Recurrent activity in Active Galactic Nuclei. *Bull. Astron. Soc. India* **2009**, *37*, 63–89.
2. Schoenmakers, A.P.; de Bruyn, A.G.; Röttgering, H.J.A.; van der Laan, H.; Kaiser, C.R. Radio galaxies with a ‘double-double morphology’—I. Analysis of the radio properties and evidence for interrupted activity in active galactic nuclei. *Mon. Not. R. Astron. Soc.* **2000**, *315*, 371–380. [[CrossRef](#)]
3. Condon, J.J. Radio emission from normal galaxies. *Annu. Rev. Astron. Astrophys.* **1992**, *30*, 575–611. [[CrossRef](#)]

4. Giacintucci, S.; O'Sullivan, E.; Clarke, T.E.; Murgia, M.; Vrtilik, J.M.; Venturi, T.; David, L.P.; Raychaudhury, S.; Athreya, R.M. Recurrent Radio Outbursts at the Center of the NGC 1407 Galaxy Group. *Astrophys. J.* **2012**, *755*, 172. [[CrossRef](#)]
5. Murgia, M.; Parma, P.; Mack, K.-H.; de Ruiter, H.R.; Fanti, R.; Govoni, F.; Tarchi, A.; Giacintucci, S.; Markevitch, M. Dying radio galaxies in clusters. *Astron. Astrophys.* **2011**, *526*, A148. [[CrossRef](#)]
6. Slee, O.B.; Roy, A.L.; Murgia, M.; Andernach, H.; Ehle, M. Four Extreme Relic Radio Sources in Clusters of Galaxies. *Astron. J.* **2001**, *122*, 1172–1193. [[CrossRef](#)]
7. Jurlin, N.; Morganti, R.; Brienza, M.; Mandal, S.; Maddox, N.; Duncan, K.J.; Shabala, S.S.; Hardcastle, M.J.; Prandoni, I.; Röttgering, H.J.A.; et al. The life cycle of radio galaxies in the LOFAR Lockman Hole field. *Astron. Astrophys.* **2020**, *638*, A34. [[CrossRef](#)]
8. Parma, P.; Murgia, M.; de Ruiter, H.R.; Fanti, R.; Mack, K.-H.; Govoni, F. In search of dying radio sources in the local universe. *Astron. Astrophys.* **2007**, *470*, 875–888. [[CrossRef](#)]
9. Quici, B.; Hurley-Walker, N.; Seymour, N. Remnant radio galaxies discovered in a multi-frequency survey. *Publ. Astron. Soc. Aust.* **2021**, *38*, e008. [[CrossRef](#)]
10. Saripalli, L.; Subrahmanyam, R.; Thorat, K.; Ekers, R.D.; Hunstead, R.W.; Johnston, H.M.; Sadler, E.M. ATLBS Extended Source Sample: The Evolution in Radio Source Morphology with Flux Density. *Astrophys. J. Suppl. Ser.* **2012**, *199*, 27. [[CrossRef](#)]
11. Brienza, M.; Morganti, R.; Harwood, J.; Duchet, T.; Rajpurohit, K.; Shulevski, A.; Hardcastle, M.J.; Mahatma, V.; Godfrey, L.E.H.; Prandoni, I.; et al. Radio spectral properties and jet duty cycle in the restarted radio galaxy 3C388. *Astron. Astrophys.* **2020**, *638*, A29. [[CrossRef](#)]
12. Clarke, T.E.; Blanton, E.L.; Sarazin, C.L.; Anderson, L.D.; Gopal-Krishna; Douglass, E.M.; Kassim, N.E. Tracing Multiple Generations of Active Galactic Nucleus Feedback in the Core of Abell 262. *Astrophys. J.* **2009**, *697*, 1481–1492. [[CrossRef](#)]
13. Giacintucci, S.; Venturi, T.; Murgia, M.; Dallacasa, D.; Athreya, R.; Bardelli, S.; Mazzotta, P.; Saikia, D.J. Radio morphology and spectral analysis of cD galaxies in rich and poor galaxy clusters. *Astron. Astrophys.* **2007**, *476*, 99–119. [[CrossRef](#)]
14. Shulevski, A.; Morganti, R.; Harwood, J.J. Radiative age mapping of the remnant radio galaxy B2 0924+30: The LOFAR perspective. *Astron. Astrophys.* **2007**, *476*, 99–119. [[CrossRef](#)]
15. Kuźmicz, A.; Jamroz, M.; Koziel-Wierzbowska, D.; Weźgowiec, M. Optical and radio properties of extragalactic radio sources with recurrent jet activity. *Mon. Not. R. Astron. Soc.* **2017**, *471*, 3806–3826. [[CrossRef](#)]
16. Brienza, M.; Godfrey, L.; Morganti, R.; Prandoni, I.; Harwood, J.; Mahony, E.K.; Hardcastle, M.J.; Murgia, M.; Röttgering, H.J.A.; Shimwell, T.W.; et al. Search and modelling of remnant radio galaxies in the LOFAR Lockman Hole field. *Astron. Astrophys.* **2017**, *606*, A98. [[CrossRef](#)]
17. Shimwell, T.W.; Röttgering, H.J.A.; Best, P.N.; Williams, W.L.; Dijkema, T.J.; de Gasperin, F.; Hardcastle, M.J.; Heald, G.H.; Hoang, D.N.; Horneffer, A.; et al. The LOFAR Two-metre Sky Survey. I. Survey description and preliminary data release. *Astron. Astrophys.* **2017**, *598*, A104. [[CrossRef](#)]
18. Knowles, K.; Cotton, W.D.; Rudnick, L.; Camilo, F.; Goedhart, S.; Deane, R.; Ramatsoku, M.; Bietenholz, M.F.; Brüggem, M.; Button, C.; et al. The MeerKAT Galaxy Cluster Legacy Survey I. Survey Overview and Highlights. *arXiv* **2021**, arXiv:2111.05673.
19. Hale, C.L.; McConnell, D.; Thomson, A.J.M.; Lenc, E.; Heald, G.H.; Hotan, A.W.; Leung, J.K.; Moss, V.A.; Murphy, T.; Pritchard, J.; et al. The Rapid ASKAP Continuum Survey Paper II: First Stokes I Source Catalogue Data Release. *arXiv* **2021**, arXiv:2109.00956.
20. Van Haarlem, M.P.; Wise, M.W.; Gunst, A.W.; Heald, G.; McKean, J.P.; Hessels, J.W.T.; de Bruyn, A.G.; Nijboer, R.; Swinbank, J.; Fallows, R.; et al. LOFAR: The LOw-Frequency ARray. *Astron. Astrophys.* **2013**, *556*, A2. [[CrossRef](#)]
21. Tingay, S.J.; Goeke, R.; Bowman, J.D.; Emrich, D.; Ord, S.M.; Mitchell, D.A.; Morales, M.F.; Booler, T.; Crosse, B.; Wayth, R.B.; et al. The Murchison Widefield Array: The Square Kilometre Array Precursor at Low Radio Frequencies. *Publ. Astron. Soc. Aust.* **2013**, *30*, e007. [[CrossRef](#)]
22. ; Gupta, Y.; Ajithkumar, B.; Kale, H.S.; Nayak, S.; Sabhapathy, S.; Sureshkumar, S.; Swami, R.V.; Chengalur, J.N.; Ghosh, S.K.; Ishwara-Chandra, C.H. The upgraded GMRT: Opening new windows on the radio Universe. *Publ. Curr. Sci.* **2017**, *113*, 707. [[CrossRef](#)]
23. Camilo, F.; Scholz, P.; Serylak, M.; Buchner, S.; Merryfield, M.; Kaspi, V.M.; Archibald, R.F.; Bailes, M.; Jameson, A.; van Straten, W.; et al. Revival of the Magnetar PSR J1622-4950: Observations with MeerKAT, Parkes, XMM-Newton, Swift, Chandra, and NuSTAR. *Astrophys. J.* **2018**, *856*, 180. [[CrossRef](#)]
24. Johnston, S.; Taylor, R.; Bailes, M.; Bartel, N.; Baugh, C.; Bietenholz, M.; Blake, C.; Braun, R.; Brown, J.; Chatterjee, S.; et al. Science with ASKAP. The Australian square-kilometre-array pathfinder. *Exp. Astron.* **2008**, *22*, 151. [[CrossRef](#)]
25. Zou, S.; Maughan, B.J.; Giles, P.A.; Vikhlinin, A.; Pacaud, F.; Burenin, R.; Hornstrup, A. The X-ray luminosity-temperature relation of a complete sample of low-mass galaxy clusters. *Mon. Not. R. Astron. Soc.* **2016**, *463*, 820–831. [[CrossRef](#)]
26. Wayth, R.B.; Lenc, E.; Bell, M.E.; Callingham, J.R.; Dwarakanath, K.S.; Franzen, T.M.O.; For, B.-Q.; Gaensler, B.; Hancock, P.; Hindson, L.; et al. GLEAM: The GaLactic and Extragalactic All-Sky MWA Survey. *Publ. Astron. Soc. Aust.* **2015**, *32*, e025. [[CrossRef](#)]
27. Lane, W.M.; Cotton, W.D.; van Velzen, S.; Clarke, T.E.; Kassim, N.E.; Helmboldt, J.F.; Lazio, T.J.W.; Cohen, A.S. The Very Large Array Low-frequency Sky Survey Redux (VLSSr). *Mon. Not. R. Astron. Soc.* **2014**, *440*, 327–338. [[CrossRef](#)]
28. Intema, H.T.; Jagannathan, P.; Mooley, K.P.; Frail, D.A. The GMRT 150 MHz all-sky radio survey. First alternative data release TGSS ADR1. *Astron. Astrophys.* **2017**, *598*, A78. [[CrossRef](#)]

29. Condon, J.J.; Cotton, W.D.; Greisen, E.W.; Yin, Q.F.; Perley, R.A.; Taylor, G.B.; Broderick, J.J. The NRAO VLA Sky Survey. *Astron. J.* **1998**, *115*, 1693–1716. [[CrossRef](#)]
30. Becker, R.H.; White, R.L.; Helfand, D.J. The VLA's FIRST Survey. *Astron. Data Anal. Softw. Syst.* **1994**, *61*, 165.
31. Lacy, M.; Baum, S.A.; Chandler, C.J.; Chatterjee, S.; Clarke, T.E.; Deustua, S.; English, J.; Farnes, J.; Gaensler, B.M.; Gugliucci, N.; et al. The Karl G. Jansky Very Large Array Sky Survey (VLASS). Science Case and Survey Design. *Publ. Astron. Soc. Pac.* **2020**, *132*, 035001. [[CrossRef](#)]
32. Clarke, T.E.; Kassim, N.E.; Brisken, W.; Helmboldt, J.; Peters, W.; Ray, P.S.; Polisensky, E.; Giacintucci, S. Commensal low frequency observing on the NRAO VLA: VLITE status and future plans. In *Ground-Based and Airborne Telescopes VI*; Hall, H.J., Gilmozzi, R., Marshall, H.K., Eds.; Society of Photo-Optical Instrumentation Engineers (SPIE) Conference Series; International Society for Optics and Photonics: Bellingham, WA, USA, 2016; Volume 9906, p. 99065B.
33. Clarke, T.E.; Perley, R.A.; Kassim, N.E.; Hicks, B.C.; Owen, F.N.; Durand, S.; Kutz, C.; Pospieszalski, M.; Weiler, K.W.; Wilson, T. The Expanded Very Large Array Low Band Upgrade. General Assembly and Scientific Symposium, E5. 2011. Available online: <https://ieeexplore.ieee.org/document/6051196> (accessed on 29 June 2021).
34. Deller, A.T.; Tingay, S.J.; Bailes, M.; West, C. DiFX: A Software Correlator for Very Long Baseline Interferometry Using Multiprocessor Computing Environments. *Publ. Astron. Soc. Pac.* **2007**, *119*, 318–336. [[CrossRef](#)]
35. Burenin, R.A.; Vikhlinin, A.; Hornstrup, A.; Ebeling, H.; Quintana, H.; Mescheryakov, A. The 400 Square Degree ROSAT PSPC Galaxy Cluster Survey: Catalog and Statistical Calibration. *Astrophys. J. Suppl. Ser.* **2007**, *172*, 561–582. [[CrossRef](#)]
36. Cotton, W.D. Obfit: A Development Environment for Astronomical Algorithms. *Publ. Astron. Soc. Pac.* **2008**, *120*, 439. [[CrossRef](#)]
37. Van Moorsel, G.; Kembell, A.; Greisen, E. AIPS Developments in the Nineties. *Astron. Data Anal. Softw. Syst. V* **1996**, *101*, 37.
38. Polisensky, E.; Lane, W.M.; Hyman, S.D.; Kassim, N.E.; Giacintucci, S.; Clarke, T.E.; Cotton, W.D.; Cleland, E.; Frail, D.A. Exploring the Transient Radio Sky with VLITE: Early Results. *Astrophys. J.* **2016**, *832*, 60. [[CrossRef](#)]
39. Perley, R.A.; Butler, B.J. An Accurate Flux Density Scale from 50 MHz to 50 GHz. *Astrophys. J. Suppl. Ser.* **2017**, *230*, 7. [[CrossRef](#)]
40. Offringa, A.R.; McKinley, B.; Hurley-Walker, N.; Briggs, F.H.; Wayth, R.B.; Kaplan, D.L.; Bell, M.E.; Feng, L.; Neben, A.R.; Hughes, J.D.; et al. WSCLEAN: An implementation of a fast, generic wide-field imager for radio astronomy. *Mon. Not. R. Astron. Soc.* **2014**, *444*, 606–619. [[CrossRef](#)]
41. Briggs, D.S. High Fidelity Interferometric Imaging: Robust Weighting and NNLS Deconvolution. Ph.D. Thesis, New Mexico Institute of Mining Technology, Socorro, NM, USA, 1995.
42. Chandra, P.; Ray, A.; Bhatnagar, S. The Late-Time Radio Emission from SN 1993J at Meter Wavelengths. *Astrophys. J.* **2004**, *612*, 974–987. [[CrossRef](#)]
43. Vikhlinin, A.; Markevitch, M.; Murray, S.S.; Jones, C.; Forman, W.; Van Speybroeck, L. Chandra Temperature Profiles for a Sample of Nearby Relaxed Galaxy Clusters. *Astrophys. J.* **2005**, *628*, 655–672. [[CrossRef](#)]
44. Markevitch, M.; Mazzotta, P.; Vikhlinin, A.; Burke, D.; Butt, Y.; David, L.; Donnelly, H.; Forman, W.R.; Harris, D.; Kim, D.-W.; et al. Chandra Temperature Map of A754 and Constraints on Thermal Conduction. *Astrophys. J.* **2003**, *586*, L19–L23. [[CrossRef](#)]
45. Markevitch, M.; Ponman, T.J.; Nulsen, P.E.J.; Bautz, M.W.; Burke, D.J.; David, L.P.; Davis, D.; Donnelly, R.H.; Forman, W.R.; Jones, C.; et al. Chandra Observation of Abell 2142: Survival of Dense Subcluster Cores in a Merger. *Astrophys. J.* **2000**, *541*, 542–549. [[CrossRef](#)]
46. Kalberla, P.M.W.; Burton, W.B.; Hartmann, D.; Arnal, E.M.; Bajaja, E.; Morras, R.; Pöppel, W.G.L. The Leiden/Argentine/Bonn (LAB) Survey of Galactic HI. Final data release of the combined LDS and IAR surveys with improved stray-radiation corrections. *Astron. Astrophys.* **2005**, *440*, 775–782. [[CrossRef](#)]
47. York, D.G.; Adelman, J.; Anderson, J.E.; Anderson, S.F.; Annis, J.; Bahcall, N.A.; Bakken, J.A.; Barkhouser, R.; Bastian, S.; Berman, E.; et al. The Sloan Digital Sky Survey: Technical Summary. *Astron. J.* **2000**, *120*, 1579. [[CrossRef](#)]
48. Lawrence, A.; Warren, S.J.; Almaini, O.; Edge, A.C.; Hambly, N.C.; Jameson, R.F.; Lucas, P.; Casali, M.; Adamson, A.; Dye, S.; et al. The UKIRT Infrared Deep Sky Survey (UKIDSS). *Mon. Not. R. Astron. Soc.* **2007**, *379*, 1599–1617. [[CrossRef](#)]
49. Chambers, K.C.; Magnier, E.A.; Metcalfe, N.; Flewelling, H.A.; Huber, M.E.; Waters, C.Z.; Denneau, L.; Draper, P.W.; Farrow, D.; Finkbeiner, D.P.; et al. The Pan-STARRS1 Surveys. *arXiv* **2016**, arXiv:1612.05560.
50. Beck, R.; Krause, M. Revised equipartition and minimum energy formula for magnetic field strength estimates from radio synchrotron observations. *Astron. Nachrichten* **2005**, *326*, 414–427. [[CrossRef](#)]
51. Brunetti, G.; Setti, G.; Comastri, A. Inverse Compton X-rays from strong FR II radio-galaxies. *Astron. Astrophys.* **1997**, *325*, 898–910.
52. Vikhlinin, A.; Burenin, R.A.; Ebeling, H.; Forman, W.R.; Hornstrup, A.; Jones, C.; Kravtsov, A.V.; Murray, S.S.; Nagai, D.; Quintana, H.; et al. Chandra Cluster Cosmology Project. II. Samples and X-ray Data Reduction. *Astrophys. J.* **2009**, *692*, 1033–1059. [[CrossRef](#)]
53. Jones, C.; Forman, W. The structure of clusters of galaxies observed with Einstein. *Astrophys. J.* **1984**, *276*, 38–55. [[CrossRef](#)]
54. Nandi, S.; Saikia, D.J.; Roy, R.; Dabhade, P.; Wadadekar, Y.; Larsson, J.; Baes, M.; Chandola, H.C.; Singh, M. A low-frequency study of recently identified double-double radio galaxies. *Mon. Not. R. Astron. Soc.* **2019**, *486*, 5158–5170. [[CrossRef](#)]
55. Pajdosz-Śmierciak, U.; Jamrozy, M.; Soida, M.; Stawarz, L. Megaparsec-scale Radio Structure Associated with a Hybrid Blazar SBS B1646+499: Episodic Jet Activity with Precessing Axis. *Astrophys. J.* **2018**, *868*, 64. [[CrossRef](#)]
56. Nandi, S.; Jamrozy, M.; Roy, R.; Larsson, J.; Saikia, D.J.; Baes, M.; Singh, M. Tale of J1328+2752: A misaligned double-double radio galaxy hosted by a binary black hole? *Mon. Not. R. Astron. Soc.* **2017**, *467*, L56–L60. [[CrossRef](#)]

57. Merritt, D.; Ekers, R.D. Tracing Black Hole Mergers through Radio Lobe Morphology. *Science* **2002**, *297*, 1310–1313. [[CrossRef](#)] [[PubMed](#)]
58. Liu, F.K.; Wu, X.-B.; Cao, S.L. Double-double radio galaxies: Remnants of merged supermassive binary black holes. *Mon. Not. R. Astron. Soc.* **2003**, *340*, 411–416. [[CrossRef](#)]
59. Nulsen, P.E.J.; McNamara, B.R.; Wise, M.W. The Cluster-Scale AGN Outburst in Hydra A. *Astrophys. J.* **2005**, *628*, 629–636. [[CrossRef](#)]
60. Simionescu, A.; Roediger, E.; Nulsen, P.E.J. The large-scale shock in the cluster of galaxies Hydra A. *Astron. Astrophys.* **2009**, *495*, 721–732. [[CrossRef](#)]
61. Birzan, L.; McNamara, B.R.; Nulsen, P.E.J.; Carilli, C.L.; Wise, M.W. Radiative Efficiency and Content of Extragalactic Radio Sources: Toward a Universal Scaling Relation between Jet Power and Radio Power. *Astrophys. J.* **2008**, *686*, 859–880. [[CrossRef](#)]
62. O’Sullivan, E.; Giacintucci, S.; David, L.P.; Vrtilik, J.M.; Raychaudhury, S. A deep Chandra observation of the poor cluster AWM 4—II. The role of the radio jets in enriching the intracluster medium. *Mon. Not. R. Astron. Soc.* **2011**, *411*, 1833–1842. [[CrossRef](#)]
63. Shin, J.; Woo, J.-H.; Mulchaey, J.S. A Systematic Search for X-ray Cavities in Galaxy Clusters, Groups, and Elliptical Galaxies. *Astrophys. J. Suppl. Ser.* **2016**, *227*, 31. [[CrossRef](#)]
64. Giacintucci, S.; Markevitch, M.; Johnston-Hollitt, M.; Wik, D.R.; Wang, Q.H.S.; Clarke, T.E. Discovery of a Giant Radio Fossil in the Ophiuchus Galaxy Cluster. *Astrophys. J.* **2020**, *891*, 1. [[CrossRef](#)]
65. Sanders, J.S.; Fabian, A.C.; Taylor, G.B. Giant cavities, cooling and metallicity substructure in Abell 2204. *Mon. Not. R. Astron. Soc.* **2009**, *393*, 71–82. [[CrossRef](#)]
66. Wise, M.W.; McNamara, B.R.; Nulsen, P.E.J.; Houck, J.C.; David, L.P. X-ray Supercavities in the Hydra A Cluster and the Outburst History of the Central Galaxy’s Active Nucleus. *Astrophys. J.* **2007**, *659*, 1153–1158. [[CrossRef](#)]
67. McNamara, B.R.; Nulsen, P.E.J. Heating Hot Atmospheres with Active Galactic Nuclei. *Annu. Rev. Astron. Astrophys.* **2007**, *45*, 117–175. [[CrossRef](#)]
68. Werner, N.; McNamara, B.R.; Churazov, E.; Scannapieco, E. Hot Atmospheres, Cold Gas, AGN Feedback and the Evolution of Early Type Galaxies: A Topical Perspective. *Space Sci. Rev.* **2019**, *215*, 5. [[CrossRef](#)]
69. Birzan, L.; Rafferty, D.A.; McNamara, B.R.; Nulsen, P.E.J.; Wise, M.W. The Detectability of AGN Cavities in Cooling-Flow Clusters. *AIP Conf. Proc.* **2009**, *1201*, 301–304.
70. O’Sullivan, E.; Giacintucci, S.; David, L.P.; Vrtilik, J.M.; Raychaudhury, S. A deep Chandra observation of the poor cluster AWM 4—I. Properties of the central radio galaxy and its effects on the intracluster medium. *Mon. Not. R. Astron. Soc.* **2010**, *407*, 321–338. [[CrossRef](#)]
71. Randall, S.W.; Forman, W.R.; Giacintucci, S. Shocks and Cavities from Multiple Outbursts in the Galaxy Group NGC 5813: A Window to Active Galactic Nucleus Feedback. *Astrophys. J.* **2011**, *726*, 86. [[CrossRef](#)]
72. O’Dea, C.P.; Owen, F.N. Astrophysical Implications of the Multifrequency VLA Observations of NGC 1265. *Astrophys. J.* **1987**, *316*, 95. [[CrossRef](#)]
73. Croston, J.H.; Hardcastle, M.J.; Birkinshaw, M.; Worrall, D.M.; Laing, R.A. An XMM-Newton study of the environments, particle content and impact of low-power radio galaxies. *Mon. Not. R. Astron. Soc.* **2008**, *386*, 1709–1728. [[CrossRef](#)]
74. Biava, N.; Brienza, M.; Bonafede, A.; Gitti, M.; Bonnassieux, E.; Harwood, J.; Edge, A.C.; Gitti, M.; Bonnassieux, E.; Harwood, J.; et al. Constraining the AGN duty cycle in the cool-core cluster MS 0735.6+7421 with LOFAR data. *Astron. Astrophys.* **2021**, *650*, A170. [[CrossRef](#)]
75. Murgia, M.; Markevitch, M.; Govoni, F.; Parma, P.; Fanti, R.; de Ruiter, H.R.; Mack, K.-H. Chandra observations of dying radio sources in galaxy clusters. *Astron. Astrophys.* **2012**, *548*, A75. [[CrossRef](#)]
76. Croston, J.H.; Hardcastle, M.J. The particle content of low-power radio galaxies in groups and clusters. *Mon. Not. R. Astron. Soc.* **2014**, *438*, 3310–3321. [[CrossRef](#)]
77. Sun, M.; Jones, C.; Forman, W.; Vikhlinin, A.; Donahue, M.; Voit, M. X-ray Thermal Coronae of Galaxies in Hot Clusters: Ubiquity of Embedded Mini-Cooling Cores. *Astrophys. J.* **2007**, *657*, 197–231. [[CrossRef](#)]
78. Cheung, C.C.; Giacintucci, S.; Clarke, T.E. Extended Radio Structures and a Compact X-ray Cool-core in the Cluster Source PKS 1353-341. *Astrophys. J.* **2019**, *875*, 108. [[CrossRef](#)]
79. Sun, M.; Forman, W.; Vikhlinin, A.; Hornstrup, A.; Jones, C.; Murray, S.S. ESO 3060170: A Massive Fossil Galaxy Group with a Heated Gas Core? *Astrophys. J.* **2004**, *612*, 805–816. [[CrossRef](#)]